Available online at www.sciencedirect.com
SCIENCE DIRECT
Journal of Catalysis 236 (2005) 251–261
JOURNAL OF CATALYSIS
www.elsevier.com/locate/jcat

Flame-spray pyrolysis preparation of perovskites for methane catalytic combustion

Gian Luca Chiarello, Ilenia Rossetti, Lucio Forni *

Dip. di Chimica Fisica ed Elettrochimica, Università degli Studi di Milano, v. C. Golgi, 19 I-20133 Milano, Italy

Received 20 July 2005; revised 22 September 2005; accepted 1 October 2005

Available online 7 November 2005

Abstract

A flame spray pyrolysis apparatus was set up and optimised for the preparation of perovskitic mixed-metal oxides in nanoparticle-size powder form. $LaCoO_3$ was chosen as test catalyst, aiming at correlating crystallinity, surface area, particle size, catalytic activity, and durability with some fundamental operating parameters of the apparatus. In particular, the feeding rate of the precursor solution, the flow rate of the O_2/CH_4 mixture for the igniter, and flow rate and linear velocity of the main dispersing-oxidising oxygen were thoroughly analysed. The activity of the prepared samples was tested for the catalytic flameless combustion of methane, a reaction requiring the proper combination of catalyst activity and thermal stability. Provided that a crystalline perovskitic phase forms, activity increases with increasing surface area of the powder. In contrast, the higher the initial sintering of catalyst particles within the flame, the higher is thermal stability. Tuning up the operating parameters allows us to properly address the desired catalyst properties.

Keywords: Flame-spray-pyrolysis; Catalytic flameless combustion of methane; $LaCoO_3$ perovskite

1. Introduction

Perovskitic mixed oxides are interesting materials for a wide variety of applications, including anodes for solid oxide fuel cells, gas sensors, and, primarily, partial or full oxidation reactions. Among these, catalytic flameless combustion (CFC) of hydrocarbons, particularly of methane, is of increasing importance for energy production. Indeed, CFC can be done at lower temperature (<800 °C) with respect to usual combustion, virtually suppressing any NO_x formation. Moreover, the catalyst strongly enhances selectivity toward full oxidation, so eliminating other noxious pollutants, such as CO and partial oxidation products.

The main catalyst requirements for CFC of methane are phase purity, ionic mobility through the crystal lattice, high surface area, and good resistance to high temperature. Satisfying all of these requirements at once is difficult. A pure perovskitic phase forms at high temperature, usually >700 °C. Hence traditional preparation methods were based on repeated cycles of calcination-milling of the precursor single oxides, leading to well-crystallised and thermally resistant materials but with very low surface areas. For this reason, this procedure is still used only for preparing ceramic materials. Many different sol–gel preparation routes have been developed in attempts to increase the surface area for catalytic use [1–8], leading to a pure perovskitic phase at lower temperature. Unfortunately, the lower the preparation temperature, the lower the thermal resistance of the material. Hence, because of ready particle sintering during use, these routes are unsuitable for high-temperature catalytic applications. Recently, high-energy mechanical milling to obtain mixed oxides through low-temperature solid-state reactions was proposed [9–11]. However, application to $LaCoO_3$ and $LaMnO_3$ did not lead to complete precursor conversion even in the presence of milling aids and for prolonged reaction time [12].

Several years ago we developed a flame hydrolysis (FH) technique that combines high surface area, and hence high catalytic activity, with good thermal stability under the high-temperature CFC working conditions [7,8,13]. The FH-prepared perovskitic catalysts had high phase purity, nanometer-sized

* Corresponding author. Fax: +39 02 50314300.
E-mail address: lucio.forni@unimi.it (L. Forni).

0021-9517/$ – see front matter
doi:10.1016/j.jcat.2005.10.003

particles, relatively high surface area (up to ca. 20 m^2/g), and exceptionally high thermal stability [7,8,13–16]. The method was based on nebulising an aqueous solution of the oxide precursors in a $H_2 + O_2$ flame. The residence time of the droplets within the flame was a few milliseconds, preventing any extensive sintering of the powder. Catalytic activity and especially thermal stability were satisfactory, and the catalysts produced were of high crystallinity and purity, with no trace of precursors or carbonaceous residua. However, the productivity was very low, just a few mg/h, and rather energy-expensive.

Many research groups have developed different flame-based techniques for the synthesis of oxides, some of which have been adopted for commercial production of SiO_2 or TiO_2 nanoparticles [17–19]. In the past, the main limitation was the availability of volatile precursors to feed to the flame. The development of aerosol or liquid-feed flame pyrolysis (FP) has overcome the low productivity problem, widely extending the applications of flame synthesis [20–39]. Among the methods proposed, spray FP seems the most interesting for the production of perovskitic oxides, because it does not require volatile precursors. It is based on a specially designed burner [20–31,39] fed with oxygen through a nozzle through which an organic solution of the precursors is also fed, with the solvent acting as the fuel for the flame. The mixture is ignited by a surrounding ring of O_2/CH_4 flamelets. High productivity and phase purity are reported, along with nanometer-sized particles and hence very high surface area (>100 m^2/g). The relatively high temperature of the flame in principle should also ensure thermal stability, once the main operating parameters have been optimised.

The aim of the present work was to set up and optimise an FP apparatus for preparing perovskitic catalysts for the CFC of methane. Attention was paid to the structural homogeneity of the product in an attempt to extend the preparation procedure now used mainly for single-oxide synthesis to mixed oxides. $LaCoO_3$ was chosen as model catalyst for system optimisation. The investigation included the effects of significant nozzle operating parameters on surface area, particle size, phase purity, crystal structure, catalytic activity for the test reaction, and thermal resistance of the catalyst. We report in detail the effects of a liquid feeding rate, of an O_2/CH_4 mixture flow rate, and of flow rate and linear velocity of the dispersing-oxidising oxygen.

2. Experimental

2.1. Precursor solution

$La(CH_3COO)_3{\cdot}2H_2O$ (Aldrich; purity >99.9%) and $Co(CH_3COO)_2{\cdot}4H_2O$ (Merck; purum), in the desired ratio and metal concentration, were dissolved in propionic acid under vigorous stirring at 60 °C.

2.2. Flame-pyrolysis apparatus

Our homemade FP apparatus is composed of three sections: (1) the flame reactor (burner), (2) the feeding rate control devices for gaseous and liquid reagents, and (3) the catalyst powder collection system. A schematic representation of this system is given in Fig. 1. The burner consists of a capillary tube (0.6 mm i.d.) ending in the centre of a vertical nozzle and connected to a syringe pump (Harvard, model 975) that feeds the solution of the mixed-oxide precursors. The nozzle is fed with oxygen (SIAD; purity 99.95%), acting as both an oxidant and a dispersing agent, so as to form very small droplets of solution. The main flame is ignited and supported by a ring of 12 premixed $O_2 + CH_4$ (SIAD; purity 99.0%) flamelets. Gas flow rate is controlled by means of MKS Instruments mass flow regulators (model 1259C), governed by a MKS control unit (model 247C). Oxygen linear velocity and pressure drop across the nozzle are varied by selecting the proper feeding rate and/or adjusting the nozzle discharge cross-section and geometry. Calibrated manometers provide for control of the oxygen inlet pressure. Another ring of small air-feeding nozzles (not shown in Fig. 1) enables maintenance of an oxidising atmosphere around the burner and helps convey the product to the powder collection section. The latter consists of a cylindric electrostatic precipitator, based on a multipin effluviator, surrounded by a coaxial collector and maintained at a 10 kV potential difference [7]. The system provided ca. 80% recovery of the produced powder.

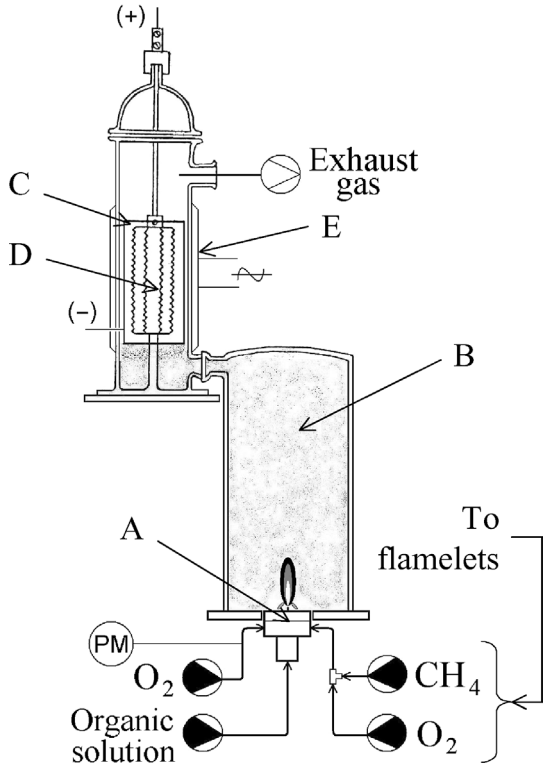

Fig. 1. Scheme of the FP apparatus. A: burner, B: pyrex glass conveyor, C: collector, D: multipin effluviator, E: heating mantle.

2.3. Catalyst characterisation

Specific surface area (SSA) was measured by N_2 adsorption/desorption at 77 K using a Micromeritics ASAP 2010 apparatus, after outgassing at 300 °C for at least 6 h. All of the recorded isotherms were of type III, indicating a nonporous

dense material. This permits a direct correlation between SSA and average particle size of the powder. Scanning electron microscopy (SEM) analysis was carried out on a Leica LEO 1430 instrument. A Philips PW1820 powder diffractometer, with Ni-filtered Cu-K_α radiation ($\lambda = 1.5148$ Å), was used for structural analysis. The diffractograms obtained were compared with literature data [40] for phase recognition. If not specifically indicated in text, no phases besides perovskite-like $LaCoO_3$ were observed.

2.4. Catalytic activity

The catalytic activity tests for the CFC of methane were carried out with a bench-scale continuous reaction unit. A quartz tubular reactor (7 mm i.d.) was heated by a tubular furnace through two heavy hemicylindrical metal blocks. The catalyst (ca. 0.2 g, 0.15–0.25 mm particle size, diluted 1:6.5 by weight with quartz powder of the same particle size) was placed in the isothermal middle part of the reactor, between two flocks of quartz wool. The void part of the reactor tube, above and below the catalyst bed, was filled with quartz beads (10–20 mesh). Before each run, the catalyst was activated in flowing air (20 cm^3/min) with the temperature increased at a rate of 10 °C/min up to 600 °C, where it was maintained for 1 h. The activity tests were carried out by feeding a mixture composed of 0.5 vol% CH_4, 49.5 vol% He, and 50 vol% air while increasing temperature by 2 °C/min from 250 °C to 600 °C. The outlet gas was analysed in line using an HP 5890 gas chromatograph, equipped with Porapak Q and MS-5 columns. The total flow rate of the gas mixture was calculated by referring to the mass of active phase, to ensure an identical value of the time factor $\tau = W/F = 2.5$ (mg of perovskite × min/cm^3 of overall gas flow rate) for each test.

2.5. Accelerated thermal deactivation tests

Accelerated thermal deactivation tests were conducted after keeping the sample at the temperature (T_f) of maximum conversion for 48 h while measuring the residual conversion every 24 h. Then reaction/deactivation cycle was accomplished by increasing temperature at a rate of 10 °C/min up to 800 °C and maintaining it there for 1 h, then dropping the temperature back to T_f and keeping it there for 3 h, at which time the catalytic activity was evaluated. The cycle was repeated at least three times.

3. Results and discussion

3.1. Principles of the FP technique

Fig. 2 provides a schematic representation of the main steps of the FP synthesis. The liquid solution containing the precursor salts is fed at constant flow rate through the capillary needle, ending 0.5 mm above the nozzle discharge mouth, so that the liquid droplets are instantaneously dispersed by the oxygen flow. This process forms very small droplets, whose

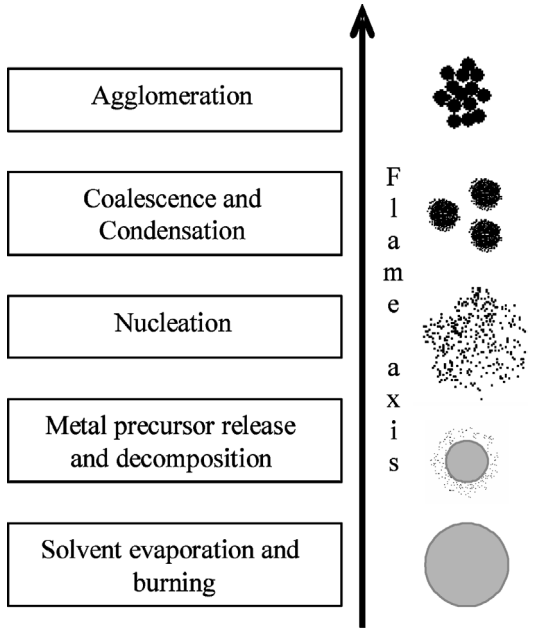

Fig. 2. Scheme of the principle of particle formation and growth into the flame.

size depends mainly on liquid and oxygen flow rate and linear velocity. Extensive studies have been carried out by Mädler et al. [39], who concentrated on the first zone of the flame, trying to model droplet dispersion and size through correlations between proper adimensional parameters. Good dispersion and short droplet lifetime were observed by using oxygen (as in the present case) rather than air as a dispersant/oxidant in the main nozzle. Keep in mind that excessively large droplets could have a lifetime longer than the residence time in the hottest zone of the flame, leading to nonuniform particle size [23].

The mechanism of product formation depends on the particular system under study. Solvent volatility is a key parameter. If the solvent readily evaporates, then product formation proceeds through monomer or cluster formation, as in aerosol processes (e.g., ZrO_2 synthesis [25]). In contrast, slow solvent evaporation can lead to the formation of "eggshell" hollow particles, which are susceptible to breakdown from the explosive evaporation of the residual solvent inside them [25,28,32]. This phenomenon can be observed with fusible precursors even in the case of rapid solvent evaporation, such as in Bi_2O_3 preparation [22].

The presence of primary solid particles at greater distances from the nozzle mouth can only be hypothesised. After this point, the main steps are coalescence (depending on collisions between the particles) and sintering. The former phenomenon can be limited by decreasing particle concentration in the flame, thereby though lowering productivity. But extensive sintering can be avoided by lowering flame temperature and decreasing particle residence time in the hottest zone. This parameter can be modulated in two ways: (1) by shortening flame height through the proper selection of O_2 feeding flow rate, and (2) by increasing O_2 linear velocity. Fig. 2 summarises some of the main parameters influencing the SSA and particle size of the product, which ultimately affect catalytic activity and thermal stability.

3.2. Optimisation of the FP apparatus

Our FP apparatus was set up following a schematic drawing published previously [39]. The main difference is the closed powder collection section, including the electrostatic precipitator (Fig. 1), which also substantially reduces the noise from the jet flame nozzle. Furthermore, in our apparatus the addition of a large air-supply nozzle ring surrounding the flame better conveys the powder to the recovery section and promotes full combustion of the organic matter, virtually eliminating any carbonaceous residua.

The first burner was fashioned with a coaxial ring (20 mm i.d.) of 12 vertical flamelets, similar to that reported previously [39]. This design produced a very unstable flame, however. Substantial improvements in flame stability and homogeneity of catalyst particle size were obtained by reducing the diameter of the flamelet ring and pointing the flamelets toward the core of the nozzle.

3.3. Effect of nozzle operating parameters on catalyst physicochemical properties

The FP technique is very versatile, with the properties of the prepared material depending on many different parameters that sometimes contrast or conflict with one another. The following are the most representative:

- O_2 and CH_4 flow rate to the supporting flamelets.
- O_2 flow rate to the main nozzle.
- Organic liquid solution flow rate.
- Concentration of precursors in the organic liquid solution.
- Pressure drop across the nozzle and nozzle geometry.
- Nature of the organic solvent and the metal precursor.

In this paper we report on only some of these parameters—$O_2 + CH_4$ gas mixture composition and flow rate for the supporting flamelets, concentration of the oxide precursors and flow rate of the liquid solution, and O_2 flow rate and pressure drop across the main nozzle.

3.3.1. O_2/CH_4 gas mixture for the supporting flamelets

The essential role of the flamelet ring is to support and constantly ignite the main flame. Initially a stoichiometric mixture of CH_4 + air was used, leading to poor flame stability when the Pyrex cap of the conveyer to the electrostatic precipitator was put in place. This problem was readily overcome by substituting oxygen for air.

As for the O_2/CH_4 feeding ratio, excessive O_2 was detrimental in all cases, leading to progressive shortening of the flamelets while increasing their flow rate until extinction. A stoichiometric feeding ratio was preferable by far.

The flamelets' overall gas flow rate had an affect on product properties. Hence, for fuel and oxygen economy, the lowest feeding rate (1 L/min of O_2 and 0.5 L/min of CH_4) providing a stable and compact crown of flamelets was chosen.

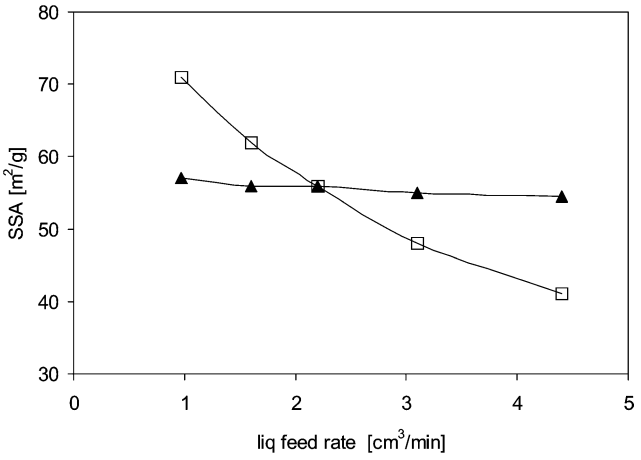

Fig. 3. Dependence of SSA on liquid flow rate. Open squares: constant (5 NL/min) O_2 flow rate; full triangles: constant O_2/liquid ($\Phi = 2$) feeding ratio.

3.3.2. Liquid flow rate

Ceteris paribus, the productivity of the system is proportional to liquid flow rate. Hence, in principle, the latter should be as high as possible. However, the higher the flow rate, the higher the concentration of the forming powder in the flame, which increases the frequency of particle collision and sintering. Hence if the goal is to obtain high surface area (i.e., poorly agglomerated products), then a compromise between productivity and particle size must be found.

Liquid flow rate was varied, either by keeping the O_2/liquid feeding ratio,

$$\Phi = \frac{(\text{mol O}_2/\text{mol fuel})_{\text{real}}}{(\text{mol O}_2/\text{mol fuel})_{\text{stoich}}},$$

at a constant value ($\Phi = 2$) or by increasing liquid flow rate at constant O_2 feeding rate (5 L/min). In the former case, the flame height remained constant (ca. 4 cm), and no significant change in product SSA was observed. Indeed, by increasing the solution flow rate from 0.97 to 4.4 cm^3/min, the BET surface area was always ca. 55 m^2/g (Fig. 3). Under these conditions, the particle concentration in the flame increases, but the particles' residence time within the flame decreases. These effects compensate for one another, producing a constant particle size. In contrast, when the liquid feeding rate was increased (vide supra) by keeping the O_2 flow rate constant at a value exceeding the stoichiometric value, productivity increased along with flame height; however, a progressive drop in product surface area (from 70 to 41 m^2/g) was observed (Fig. 3) due to the increased particle concentration within the flame.

It can be concluded that if the goal is a high-productivity preparation of highly sintered materials, then the liquid flow rate must be enhanced by maintaining a constant O_2 feeding rate. In contrast, the productivity of high-surface area catalysts can be improved by increasing the solution flow rate while keeping the O_2/liquid feeding ratio constant.

3.3.3. Concentration of the precursors solution

Obviously, the higher the precursors concentration, the higher is the amount of powder produced per unit time. Hence,

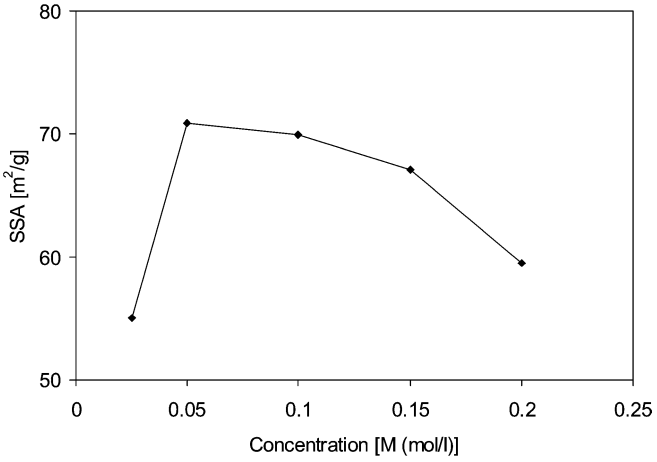

Fig. 4. Dependence of SSA on precursors concentration M (mol/L) in the feeding solution.

to save time, solvent, O_2 and auxiliary gases, highly concentrated solutions are preferable, of course within the precursor solubility limits. However, when increasing the precursors concentration beyond a given limit, a noticeable drop in surface area can be observed (Fig. 4). This is due to an increased concentration of primary particles in the flame, which favours frequent particle collision and sintering. Furthermore, the increased availability of precursors could also enhance sintering in the gas phase, leading to particle necking. Hence diluted solutions are preferable for preparing small, high-surface area particles by increasing productivity through a liquid flow rate adjustment at constant Φ (vide supra). The first point in Fig. 4 (i.e., for a concentration of 0.025 M) is due to the formation of overly small primary particles, which sinter more easily in the hottest zone of the flame.

A tentative calculation of the theoretical size of a particle can be done by hypothesising an instantaneous evaporation of the solvent of a single droplet. The resulting particle should have a diameter, D_p, given by

$$D_p = D_d \sqrt[3]{M \cdot N_A \cdot V_{uc}/Z},$$

where D_d is the droplet diameter, M is the molar concentration, N_A is Avogadro's number, V_{uc} is the crystal unit cell volume (336.13 Å^3 for $LaCoO_3$), and Z is the number of molecules per unit cell (6 for $LaCoO_3$).

For $D_d = 4$ μm (a reasonable value for a spray droplet) and $M = 0.1$ mol/L, the resulting D_p should be 600 nm, rather far from our experimental evidence of BET average particle diameter (D_{BET}) ≈ 12–20 nm ($D_{BET} = 6/SSA \cdot \rho$ and $\rho =$ 7.29 g/mL for $LaCoO_3$). In other words, the droplet diameter must be unreasonably low (by 1 or 2 orders of magnitude) to lead to the observed D_{BET} value. Therefore, it can be concluded that our product particles derive from secondary droplets forming through dispersion of the primary droplets by oxygen. Alternatively, small particles could form by the breaking of primary hollow particles due to evaporation of the encapsulated residual solvent [28,32], although this is less likely in the present case.

3.3.4. O_2 linear velocity

A preliminary study of the nozzle was carried out to determine its main working parameters, including the discharge coefficient, C, and the equivalent discharge section, A_{eq}, from which the O_2 linear speed in the nozzle throat may be determined under different working conditions. The mass flow rate of discharge (w) of a perfect gas from a nozzle under subcritical (subsonic) flow conditions can be calculated from the following equation [41]:

$$w = CYA_2 \sqrt{\frac{2g_c(p_1 - p_2)\rho_1}{1 - \beta^4}}, \tag{1}$$

where C is the discharge coefficient, which is a function of Reynolds number (Re) and nozzle geometry; A_2 is the cross-sectional area of the throat; p_1 and p_2 are the upstream and downstream pressure, respectively; β is the ratio of nozzle throat to adduction conduit diameter; and Y is the expansion factor. For gaseous fluids, Y is given by

$$Y = \sqrt{r^{2k}\left(\frac{k}{k-1}\right)\left(\frac{1 - r^{(k-1)/k}}{1 - r}\right)\left(\frac{1 - \beta^4}{1 - \beta^4 r^{2/k}}\right)}, \tag{2}$$

where r is the pressure ratio, p_2/p_1, and k is the specific heat ratio, c_p/c_v.

Raising the absolute upstream pressure, p_1, the discharge velocity from the nozzle increases until it attains and then overcomes the speed of sound, when the upstream pressure exceeds a critical value and the geometry of the nozzle becomes convergent–divergent. At the critical value, the pressure ratio assumes its minimum value, r_c, and the actual pressure in the throat cannot fall below $p_1 r_c$, even if a much lower pressure exists downstream. Under critical flow conditions, the mass flow rate of discharge (w_{max}) of a perfect gas can be calculated by the following equation [41]:

$$w_{max} = CA_2 p_1 \sqrt{g_c k \left(\frac{M}{RT_1}\right)\left(\frac{2}{k+1}\right)^{(k+1)/(k-1)}} = KCA_2 p_1, \tag{3}$$

where $g_c = 980$ cm/s^2, M is the gas molecular weight, T_1 is the gas temperature (K) in the upstream side of the nozzle, and R is the gas constant. For oxygen $k = 1.396$ and $r_c = 0.528$ and at room temperature, Eq. (3) becomes

$$w_{max} = 14.5CA_2 p_1, \tag{4}$$

with w_{max} expressed in g/min, A_2 in mm^2 and p_1 in bar.

Eq. (1) shows that the mass flow rate under subsonic conditions is proportional to $p_1^{1/2}$, whereas at the sonic regime it is directly proportional to p_1, as in Eq. (4). Finally, a simple equation for calculating the discharge velocity (u_2) from a convergent–divergent nozzle, given the upstream pressure (p_1), downstream pressure (p_2), and the critical velocity in the throat (u_c), is [41]

$$\left(\frac{u_2}{u_c}\right)^2 = \left(\frac{k+1}{k-1}\right)\left[1 - \left(\frac{p_2}{p_1}\right)^{(k-1)/k}\right]. \tag{5}$$

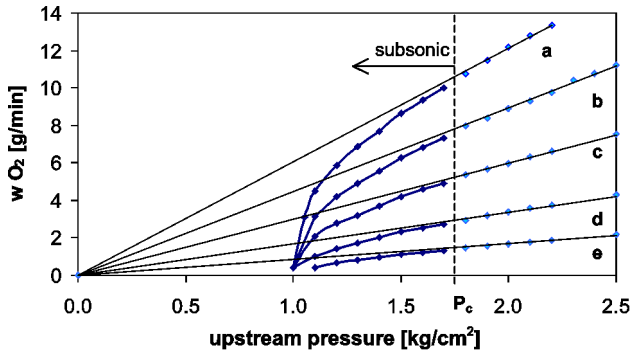

Fig. 5. Oxygen mass flow rate vs. nozzle upstream pressure (p_1) for different nozzle geometries (openings) ensuring 5 NL/min of oxygen volumetric flow rate with a pressure drop Δp across the nozzle of: (a) 0.3, (b) 1.2, (c) 3.0, (d) 4.5, (e) 6.0 bar.

Table 1
Main working parameters vs. pressure drop for a selected nozzle geometry (O_2 flow rate = 5 NL/min)

	Δp (bar)						
	0.3	0.6	1.2	3	4.5	6	7
Slope	6.057	–	3.096	1.776	1.236	0.949	–
A_{eq}[a] (mm^2)	0.418	0.281	0.213	0.116	0.085	0.065	–
p_1 (bar)	1.3	1.6	2.2	4.0	5.5	7.0	8.0
v_{max}[b] (L/min)	5.00	5.00	4.27	2.40	1.72	1.35	1.18
u[b] (m/s)	199	296	337	340	338	344	340
u_0 (m/s)	199	296	337	340	338	550	564

[a] $A_{eq} = CA_2$.
[b] In the nozzle throat.

First, a series of experimental data was collected (Fig. 5) for several different nozzle geometries (openings), maintaining the O_2 flow rate constant at 5 NL/min and varying the pressure drop, ΔP, across the nozzle (Table 1).

The discharge coefficient, C, may be calculated in one of two ways, through either Eq. (1) or Eq. (4). As an example, we report the calculation of C for the maximum nozzle opening (Fig. 5, curve a). Following the first approach, an O_2 flow rate of 5 NL/min (6.65 g/min) corresponds to an upstream pressure of 1.3 bar, lower than the critical pressure (1.8 bar). Hence the relationship between w and p_1 can be calculated by Eq. (1), applicable to subsonic flow conditions, provided that Y has been calculated through Eq. (2). Our nozzle has a crown circular cross-sectional area A, so that to calculate β, we introduce an equivalent diameter,

$$D_e = \sqrt{\frac{4A}{\pi}},$$

from which

$$\beta = \frac{D_{e2}}{D_{e1}} = \sqrt{\frac{A_2}{A_1}} = 0.23,$$

where A_1 is the cross-sectional area of the nozzle upstream conduit, before the throat. Then, from Eq. (2), we get $Y = 0.87$ and, from Eq. (1), $C = 0.41$ (at room temperature).

In the second approach, referring to sonic flow rate (Eq. (4)), the slope ($14.5CA_2$) of the linear part of the Fig. 5 experimental curves is proportional to the cross-sectional area of the so-called vena contracta (CA_2). Then, for the known value of $A_2 = 0.98$ mm^2, a value of

$$C = \frac{\text{Slope}}{14.5A_2} = \frac{A_{eq}}{A_2} = \frac{0.418}{0.98} = 0.42$$

is obtained from the slope of the straight line portion of curve a in Fig. 5 and Table 1. Then the O_2 discharge velocity can be easily calculated as actual flow rate in the throat (v_{max}) divided by the equivalent cross-sectional area (A_{eq}) (Table 1).

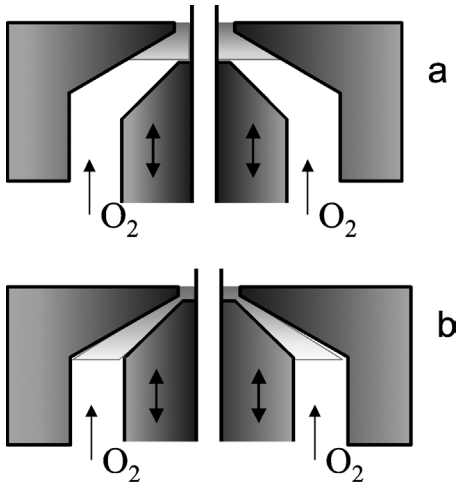

Fig. 6. Schematic representation of nozzle geometry: (a) convergent; (b) convergent–divergent.

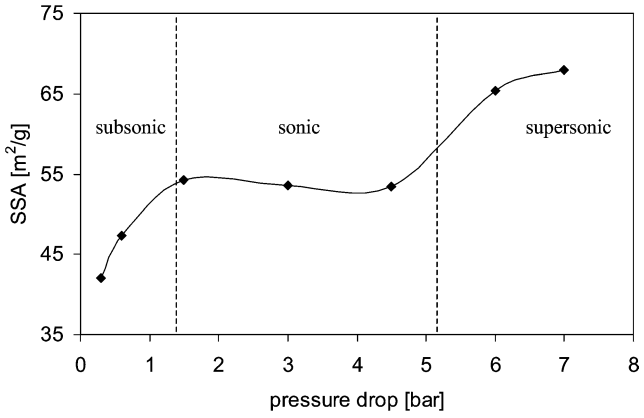

Fig. 7. Dependence of SSA on pressure drop across the nozzle.

Nozzle geometry is represented in Fig. 6, showing how the configuration can be shifted from convergent to convergent–divergent by simply moving the inner part of the burner set vertically. For a convergent nozzle (Fig. 6a), the highest obtainable discharge velocity is sonic (i.e., 341 m/s), whereas for the convergent–divergent geometry (Fig. 6b), a supersonic velocity can be attained.

Here O_2 velocity was varied at a constant O_2 flow rate by progressively narrowing the nozzle discharge section, thus increasing the pressure drop across the nozzle from 0.3 to 7 bar. The effect of O_2 discharge velocity on catalyst SSA is reported in Fig. 7. At first, under subsonic discharge conditions, an increase in SSA occurred. When sonic velocity was

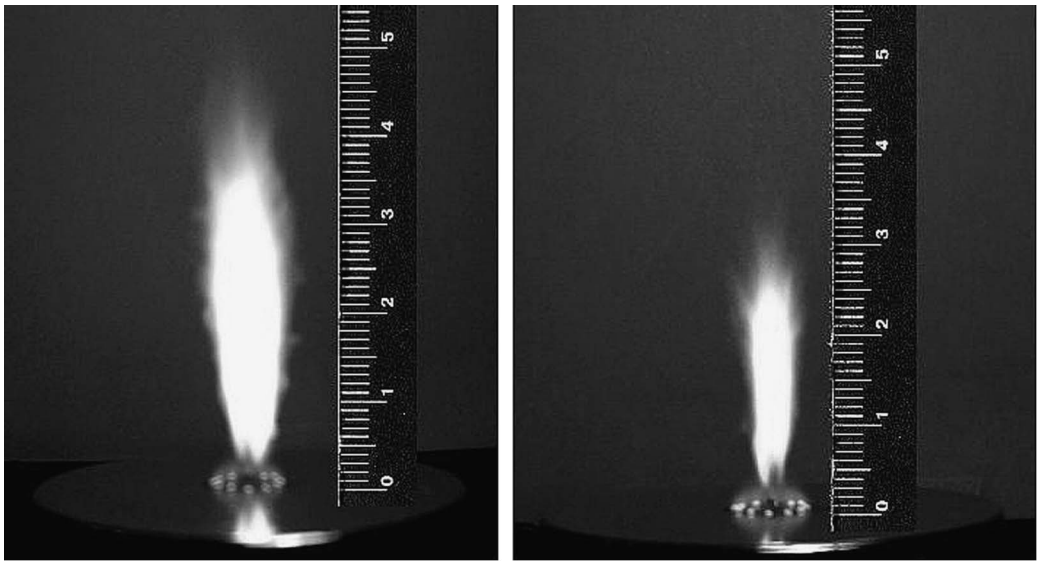

Fig. 8. Flame height in laminar (left side) or turbulent (right side) regime.

reached, a further O_2 pressure drop did not entail an increase in SSA, which remained constant, given the constant discharge linear velocity. Then, with progressive narrowing of the nozzle discharge section, its geometry changed into convergent–divergent, allowing increased O_2 linear velocity over the sonic value and hence further increasing the SSA of the product. These data were confirmed by X-ray diffraction (XRD) analysis, which showed a progressively smaller powder crystal size with increasing O_2 velocity. However, when sonic discharge conditions were kept constant, the XRD line broadening (powder crystal size) remained fairly constant.

O_2 linear velocity mainly determines the residence time of the primary particles in the flame. The lower the residence time, the lower the particle sintering and hence the higher the SSA. However, a too low residence time in the flame could lead to an insufficiently thermal-resistant powder. Moreover, the permanence of the precursor into the flame must be sufficient to permit its complete conversion into the desired perovskitic phase and the complete combustion of the organic compounds (solvent and precursor anions). O_2 velocity can be modelled throughout the flame as reported previously [23], demonstrating increased velocity immediately after the nozzle mouth (up to ca. 1.5 cm) due to combustion, followed by asymptotic deceleration, as in cold jets, as a function of $1/x$, where x is the distance from the nozzle.

Increased O_2 velocity also produces a decrease in flame height (as shown in Fig. 8), affecting the residence time in the flame. Thus O_2 velocity has a double influence on this fundamental parameter. Furthermore, images (not reported here) obtained with a high-speed infrared camera suggested a transition from a laminar to a turbulent flow regime with increased pressure drop (and hence O_2 velocity) from 0.3 to 6 bar, as evidenced by the formation of vortices. This noticeably affected SSA, which increased from 42 to 66 m^2/g. However, the most significant impact was on particle size distribution (Fig. 9). Poor size uniformity was obtained in a laminar flow regime, with SEM micrographs showing large spheres together with much smaller particles (Fig. 9a,b). In contrast, a much higher size uniformity was exhibited in a turbulent flow regime (Fig. 9c,d), with the product consisting of nanospheres ca. 20 nm in diameter. This can be explained by considering the gas velocity profile under laminar and turbulent flow conditions. In the former regime, particle residence time in the hottest part of the flame is different for primary particles in the jet core than for particles in the periphery of the jet, and no efficient mixing can occur. Under turbulent conditions, the much more efficient mixing leads to uniform residence time in any part of the jet, preventing extensive sintering of the particles. Similar behaviour was observed during the preparation of V–Ti oxide through aerosol flame synthesis [30].

3.3.5. *O_2 flow rate*

O_2 flow rate was first varied at constant nozzle discharge section, so as to create an increasing pressure drop across the nozzle. Increasing the O_2 flow rate starting from subcritical conditions produced an increasing O_2 linear velocity until critical pressure (and hence sonic discharge velocity) were attained (vide supra). The SSA of the powder rapidly increased with increasing O_2 flow rate (and velocity) (Fig. 10, full line). After the sonic regime was attained, some marginal increase of SSA was observed, but much less marked than that under subsonic conditions.

The dependence of SSA (and hence of particle size) on O_2 flow rate is rather complex. With constant nozzle geometry and under subsonic conditions, an increase in O_2 flow rate brings about an increase in its linear velocity. Therefore, an increase of SSA can be surely attributed to the aforementioned causes, that is, faster transport of the primary particles through a progressively shorter flame, which prevents any significant particle sintering. However, increasing oxygen flow rate at constant liquid feeding rate leads also to a higher dispersion degree of the particles within the flame, decreasing the probability of collision between them. Furthermore, O_2 has also a quenching

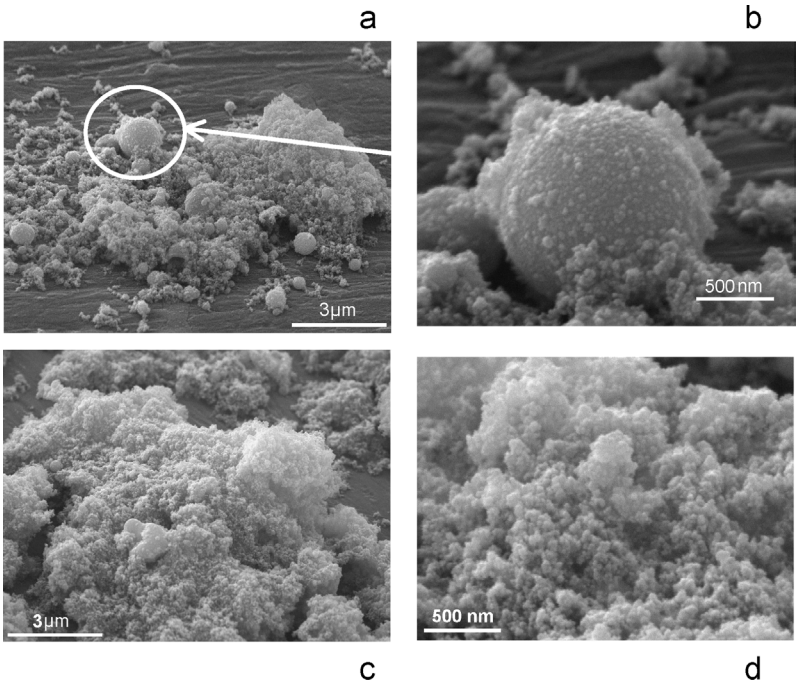

Fig. 9. Typical SEM micrographs relative to samples prepared in laminar (a, b) or turbulent (c, d) regime.

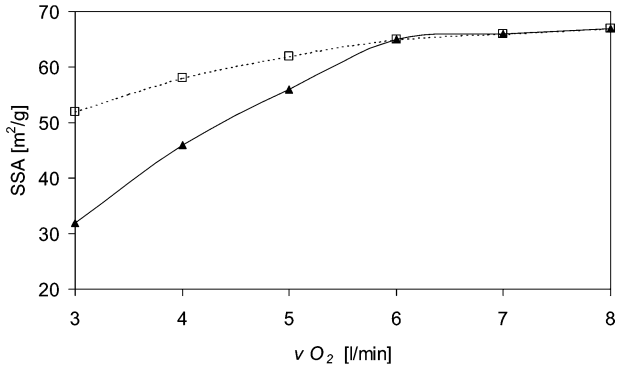

Fig. 10. SSA vs. O_2 flow rate: at constant nozzle geometry (—) or at constant pressure drop under sonic discharge conditions (- - -).

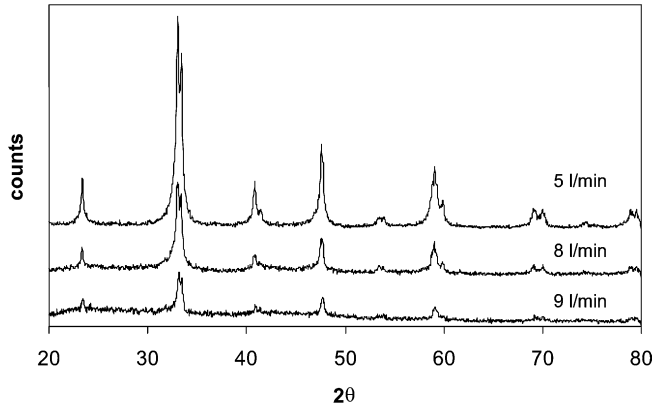

Fig. 11. Effect of O_2 flow rate (L/min) on sample crystallinity.

effect, lowering the flame temperature and hence decreasing the particle sintering rate.

Because all of these effects are hardly distinct from one another, another set of samples was prepared, this time trying to eliminate the effect of residence time on SSA and particle size. For this purpose, we varied the O_2 flow rate, but kept the pressure drop through the nozzle constant at a value higher than the critical pressure. This corresponds to sonic discharge conditions and hence to constant O_2 velocity, independent of O_2 flow rate. By increasing the latter, a small increase of surface area was observed (Fig. 10, dashed line), due exclusively to the quenching effect of oxygen and the decreased particle concentration in the flame. As expected, the two curves overlapped (Fig. 10) when sonic conditions occurred in the two cases.

It may be concluded that O_2 flow rate is a very critical parameter in obtaining the desired product, apart from its actual physical properties. Indeed, when the O_2 flow rate was too high with respect to the liquid flow rate (i.e., >8 L/min, corresponding to $\Phi > 3$), the quenching effect was excessive, inhibiting the formation of a highly crystalline perovskitic phase. The effect of this parameter on sample crystallinity is shown in Fig. 11, which qualitatively depicts the decreasing crystal size with increasing O_2 flow rate.

3.4. Effect of nozzle operating parameters on catalytic activity

The present samples were tested as catalysts for the CFC of methane. As expected, catalytic activity increased with increasing SSA, provided that a pure perovskitic phase was obtained. Catalytic performance was essentially intrafacial [1,2], as has been reported for $LaCoO_3$ samples [8,13,42]. In principle, high SSA should enhance suprafacial activity; that is, it should increase the reactivity due to available surface oxygen. Conversely, intrafacial activity should be more tied to oxygen mobility through the bulk. Oxygen mobility for undoped perovskitic systems is ultimately due to lattice disorder (i.e., the

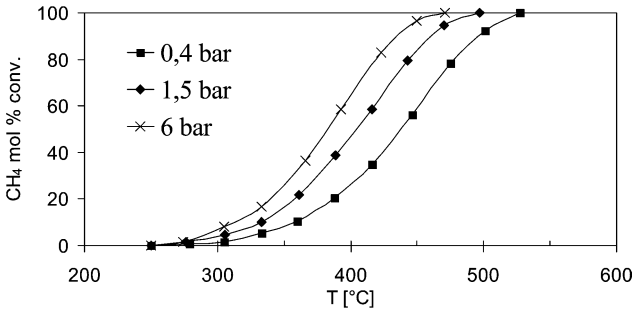

Fig. 12. Catalytic activity of samples prepared at different O_2 pressure drop (bar) across the nozzle.

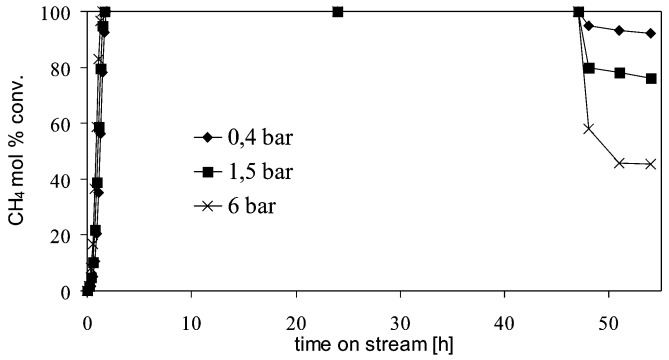

Fig. 13. Thermal stability of samples prepared at different O_2 pressure drop (bar) across the nozzle.

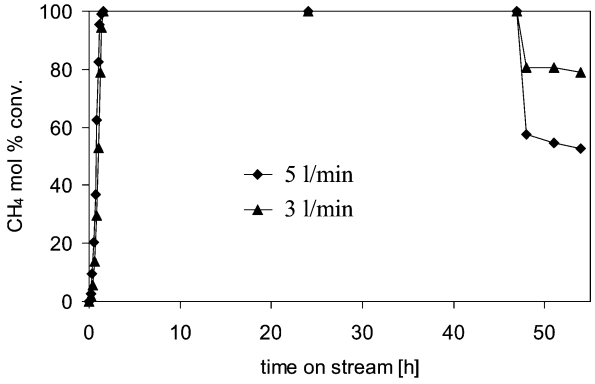

Fig. 14. Thermal stability of samples prepared at different O_2 flow rate (L/min).

presence of vacancies), allowing oxygen jumping between them with low activation energy. Therefore, synthesis conditions allowing small crystal size (i.e., high SSA) could also enhance bulk oxygen mobility.

As an example, Fig. 12 shows the dependence of catalytic activity on pressure drop (Δp) across the nozzle, and hence on O_2 discharge velocity. It can be seen that raising Δp results in noticeably enhanced catalytic activity, in line with the observed parallel increase of SSA. Indeed, the temperature of methane half conversion ($T_{1/2}$) decreased from 437 to 404 °C and then to 383 °C for Δp of 0.3, 1.5, and 6 bar, respectively.

From these activity data, we can conclude that the FP technique allows one to obtain highly active catalysts that completely convert methane below 550 °C. These results are comparable to those previously reported for some of the most active perovskitic samples obtained through other preparation techniques [7,12,13] and also to those of noble metal-based catalysts for the same reaction.

3.5. *Effect of nozzle operating parameters on catalyst thermal stability*

Because of the elevated working temperature, the CFC of methane requires a highly thermally resistant catalyst. A flame-based preparation technique can fulfil this requirement, producing rapid calcination of the powder at high temperature (>1000 °C). Thermal resistance of the present catalysts was checked both after a prolonged working time (48 h) and after cycles of accelerated deactivation at 800 °C. Once a pure perovskitic phase was formed, catalyst durability always increased with decreasing SSA. A first example of this is reported in Fig. 13, which shows the dependence of this parameter on samples prepared at different pressure drops across the nozzle and hence at different O_2 linear velocities. As mentioned earlier, the lower the pressure drop, the lower the O_2 velocity and hence the higher the reagent residence time in the flame, leading to more-sintered, lower-SSA materials. This reflects on thermal stability, which was higher for the samples prepared at lower O_2 velocity. Indeed, for the sample prepared at a pressure drop of 0.3 bar, the residual CH_4 conversion after the third deactivation cycle was still ca. 92%, much better than that of the sample synthesised with a pressure drop of 6 bar, which lost ca. 50% of its activity. Hence, as expected, improve thermal stability requires an increase in particle sintering, although at the expense of lower activity.

The same behaviour was exhibited by samples prepared with different O_2 flow rates, as reported in Fig. 14. Also in this case, an increase in O_2 flow rate from 3 to 5 L/min brought an increase in SSA from 32 to 56 m^2/g (vide supra) due to many concomitant effects (i.e., increased O_2 speed and hence decreased residence time in the flame, higher quenching, lower concentration of the primary particles in the flame). This was reflected in the much lower thermal stability of the catalyst, which lost 50% of its activity even after the first deactivation cycle when prepared with 5 L/min of oxygen.

A direct measurement of catalyst properties after the CFC reaction is not possible due to the presence of the diluting quartz powder large excess. Hence, a simulation of the effect of catalyst deactivation due to sintering was carried out by heating up to 900 °C for 2 h in air a high-surface area sample, prepared from a 0.05 M propionic acid solution (liquid flow rate = 1 cm^3/min, O_2 flow rate = 5 L/min, $\Delta P = 5$ bar). SSA dropped from >70 to <5 m^2/g. Particle sintering is clearly shown in Fig. 15 and is confirmed by the increased crystallinity evidenced in Fig. 16.

4. Conclusions

A spray FP apparatus was set up for the preparation of mixed oxides of perovskitic structure. Some different burner configurations were tested to optimise efficiency and flame stability and

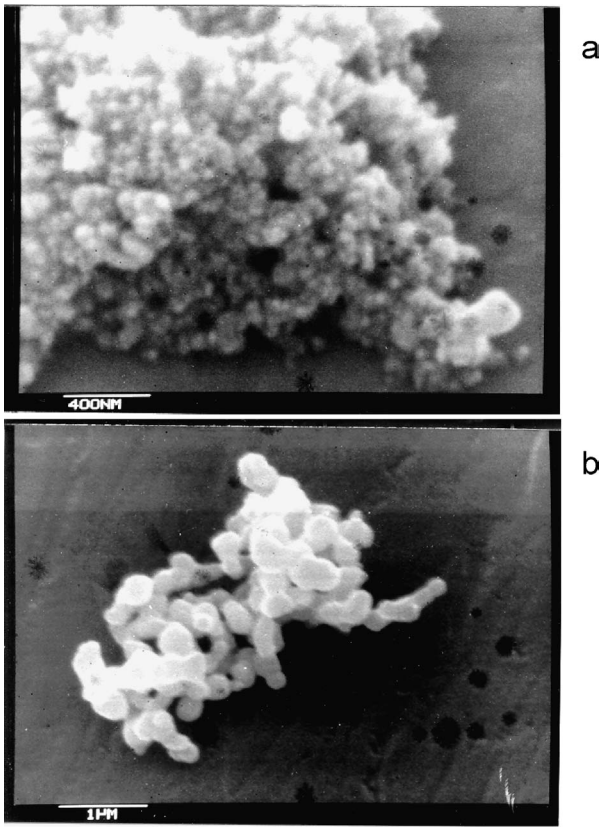

Fig. 15. Typical SEM micrographs of a high SSA sample, (a) as-prepared, (b) calcined at 900 °C for 2 h.

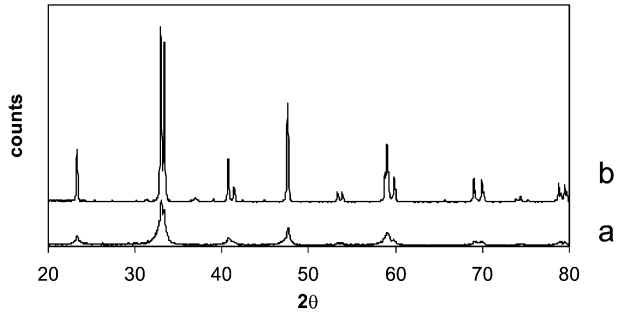

Fig. 16. XRD patterns of the Fig. 15 high SSA sample, (a) as-prepared, (b) calcined at 900 °C for 2 h.

to reduce the noise from the jet flame. The effect of some nozzle operating parameters on phase purity, surface area, and particle size of $LaCoO_3$ test samples was investigated. A substantial increase in catalyst SSA can be obtained by decreasing the concentration of the feeding solution (albeit at the cost of decreased productivity). The latter can be improved by increasing liquid flow rate, provided that the O_2/liquid feeding ratio is kept constant, so that SSA of the product is only marginally affected. A theoretical study on our nozzle allowed us to determine the O_2 discharge velocity and observe how it affects SSA. The latter increases with increasing O_2 speed under subsonic conditions, remains constant under a sonic regime, and finally increases again when a supersonic discharge velocity is reached. O_2 flow rate was varied either by increasing pressure drop (Δp) across the nozzle or by varying the nozzle geometry at constant Δp.

Table 2
Effect of the investigated operating parameters on some properties of the catalyst

Increasing of	SSA	Particle size	Crystallinity	Catalytic activity	Thermal stability
Liquid flow rate					
Const. ϕ	≈	≈	≈	≈	≈
Const. O_2 flow rate	↓	↑	↑	↓	↑
Solution concentration	↓[a]	↑	↑	↓	↑
O_2 linear velocity	↑	↓	↓	↑	↓
O_2 flow rate					
Below P_c	↑	↓	↓	↑	↓
Above P_c[b]	≈	≈	≈	≈	≈

Note: $\Phi = \frac{(\text{mol } O_2/\text{mol fuel})_{\text{real}}}{(\text{mol } O_2/\text{mol fuel})_{\text{stoich}}}$; P_c = nozzle critical pressure; ≈ = almost no effect.
[a] For concentration ⩾0.05 M.
[b] For $\phi > 3$ too low crystallinity was observed.

It was found that O_2 flow rate deeply influences both particle size and crystallinity, due to several concomitant factors. Furthermore, as expected, any change in catalyst properties deeply affects both catalytic activity for the CFC of methane and thermal resistance of the catalyst.

Table 2 provides a quick reference on effects of the various parameters investigated here on catalyst properties.

References

[1] J.L.G. Fierro, J.M.D. Tascòn, L.G. Tejuca, J. Catal. 93 (1985) 83.
[2] R.J.H. Voorhoeve, J.P. Remeika, D.W. Johnson, Science 180 (1973) 62.
[3] T. Seiyama, in: L.G. Tejuca, J.L.G. Fierro (Eds.), Properties and Applications of Perovskite-Type Oxides, Dekker, New York, 1993, p. 215.
[4] Y. Teraoka, H.M. Zhang, N. Yamazoe, Chem. Lett. (1985) 1367.
[5] Y. Teraoka, M. Yoshimatsu, N. Yamazoe, T. Seiyama, Chem. Lett. (1984) 893.
[6] H.M. Zhang, Y. Shimizu, Y. Teraoka, N. Miura, N. Yamazoe, J. Catal. 121 (1990) 432.
[7] R.A.M. Giacomuzzi, M. Portinari, I. Rossetti, L. Forni, in: A. Corma, F.V. Melo, S. Mendioroz, J.L.G. Fierro (Eds.), Study of Surface Science and Catalysis, vol. 130, Elsevier, Amsterdam, 2000, p. 197.
[8] R. Leanza, I. Rossetti, L. Fabbrini, C. Oliva, L. Forni, Appl. Catal. B: Environ. 28 (2000) 55.
[9] V. Szabo, M. Bassir, A. Van Neste, S. Kaliaguine, Appl. Catal. B: Environ. 37 (2002) 175.
[10] US Patent no. 6,017,504 (2000), to Université Laval (Canada).
[11] V. Szabo, M. Bassir, A. Van Neste, S. Kaliaguine, Appl. Catal. B: Environ. 43 (2003) 81.
[12] E. Campagnoli, A. Tavares, L. Fabbrini, I. Rossetti, Yu.A. Dubitsky, A. Zaopo, L. Forni, Appl. Catal. B: Environ. 55 (2005) 133.
[13] I. Rossetti, L. Forni, Appl. Catal. B: Environ. 33 (2001) 345.
[14] L. Fabbrini, I. Rossetti, L. Forni, Appl. Catal. B: Environ. 44 (2003) 107.
[15] L. Fabbrini, I. Rossetti, L. Forni, Appl. Catal. B: Environ. 56 (3) (2005) 221.
[16] L. Fabbrini, I. Rossetti, L. Forni, Appl. Catal. B: Environ., submitted.
[17] W.R. Moser, J.D. Lennhoff, J.E. Cnossen, K. Fraska, J.W. Schoonover, J.R. Rozak, in: W.R. Moser (Ed.), Advanced Catalysts and Nano Structured Materials, Academic Press, New York, 1996, p. 535.
[18] J. Long, S.J. Teichner, Rev. Hautes Temper. Refract. 2 (1965) 47.
[19] M. Formenti, F. Juillet, P. Meriaudeau, S.J. Teichner, P. Vergnon, J. Colloid Interface Sci. 39 (1) (1972) 79.
[20] W.J. Stark, L. Mädler, S.E. Pratsinis, EP 1,378,489 A1 (2004), to ETH, Zurich.

[21] H. Schultz, W.J. Stark, M. Maciejewski, S.E. Pratsinis, A. Baiker, J. Mater. Chem. 13 (2003) 2979.
[22] L. Mädler, S.E. Pratsinis, J. Am. Ceram. Soc. 85 (7) (2002) 1713.
[23] M.C. Heine, S.E. Pratsinis, Ind. Eng. Chem. Res., ASAP Article, web release date: March 24th, 2005.
[24] R. Strobel, W.J. Stark, L. Mädler, S.E. Pratsinis, A. Baiker, J. Catal. 213 (2003) 296.
[25] R. Mueller, R. Jossen, H.K. Kammler, S.E. Pratsinis, M.K. Akhtar, AIChE J. 50 (12) (2004) 3085.
[26] T. Tani, K. Takatori, S.E. Pratsinis, J. Am. Ceram. Soc. 87 (3) (2004) 365.
[27] R. Strobel, S.E. Pratsinis, A. Baiker, J. Mater. Chem. 15 (2005) 605.
[28] W.J. Stark, L. Mädler, M. Maciejewski, S.E. Pratsinis, A. Baiker, Chem. Commun. (2003) 588.
[29] R. Mueller, R. Jossen, S.E. Pratsinis, M. Watson, M.K. Akhtar, J. Am. Ceram. Soc. 87 (2) (2004) 197.
[30] W.J. Stark, K. Wegner, S.E. Pratsinis, A. Baiker, J. Catal. 197 (2001) 182.
[31] R. Jossen, S.E. Pratsinis, W.J. Stark, L. Mädler, J. Am. Ceram. Soc. 88 (2005) 1388.
[32] K.Y. Jung, Y.C. Kang, Mater. Lett. 58 (2004) 2161.
[33] S. Kim, J.J. Gislason, R.W. Morton, X.Q. Pan, H.P. Sun, R.M. Laine, Chem. Mater. 16 (2004) 2336.
[34] J. Marchal, T. John, R. Baranwal, T. Inklin, R.M. Laine, Chem. Mater. 16 (2004) 822.
[35] T. Johannessen, S. Koutsopoulos, J. Catal. 205 (2002) 404.
[36] J.M. Mäkelä, H. Keskinen, T. Forsblom, J. Keskiken, J. Mater. Sci. 39 (2004) 2783.
[37] A. Kilian, T.F. Morse, Aerosol Sci. Technol. 34 (2001) 227.
[38] D.J. Seo, S.B. Park, Y.C. Kang, K.L. Choy, J. Nanopart. Res. 5 (2003) 199.
[39] L. Mädler, H.K. Kammler, R. Mueller, S.E. Pratsinis, J. Aerosol Sci. 33 (2002) 369.
[40] Advanced Selected Powder Diffraction Data, Miner. DBM (1–40), J.C.P.D.S., Swarthmore, PA, 1974–1992.
[41] R.H. Perry, C.H. Chilton (Eds.), Chemical Engineer's Handbook, fifth ed., McGraw Hill, New York, 1973.
[42] E. Campagnoli, A.Tavares, L. Fabbrini, I. Rossetti, Yu.A. Dubitsky, A. Zaopo, L. Forni, J. Mater. Sci., in press.